Available online at www.sciencedirect.com

ScienceDirect

Advances in Space Research 73 (2024) 2816–2830

ADVANCES IN SPACE RESEARCH (a COSPAR publication)

www.elsevier.com/locate/asr

Towards understanding time variations of proton to helium ratios in the heliosphere: Implication for the time dependence of the elements of the diffusion tensor

M.D. Ngobeni [a,*], M.S. Potgieter [b], O.P.M. Aslam [c]

[a] Centre for Space Research, North-West University, Potchefstroom, South Africa
[b] Institute for Experimental and Applied Physics (IEAP), Christian-Albrechts-University in Kiel, Germany
[c] School of Mathematics and Statistics, University of Glasgow, Glasgow G12 8QQ, UK

Received 20 May 2023; received in revised form 6 November 2023; accepted 10 December 2023
Available online 20 December 2023

Abstract

A comprehensive three-dimensional numerical model for the modulation of cosmic rays in the heliosphere is applied to investigate the relative roles of the time dependence of the elements of the diffusion tensor on the proton to total Helium (p/He) and Helium-3 to Helium-4 ($^3He_2/^4He_2$) ratios at rigidities below 3 GV. At these rigidities the ratios have been observed by both PAMELA and AMS-02 detectors to have a time variation in response to changing solar activity. We found that the contribution of the time dependence of the perpendicular diffusion in the radial direction of the heliosphere is the dominant cause of this observed time variation, especially in the $A < 0$ magnetic field cycle, and not any fundamental difference between the solar modulation of galactic protons and He-isotopes. It follows that neglecting this time dependence from numerical models, both in value and its rigidity dependence, would produce time trends in the mentioned ratios that are incompatible with observed trends at the Earth. Furthermore, we found differences in the computed time trends of p/He and $^3He_2/^4He_2$ ratios at rigidities below 1.5 GV. This is mainly a consequence of an interplay between perpendicular diffusion in the radial direction and adiabatic energy losses which begin to influence modulated spectra at a higher rigidity for $^3He_2$ than for $^4He_2$, and for total He than for protons.

Keywords: Cosmic rays; Helium isotopes; Solar modulation; Solar activity

1. Introduction

Galactic cosmic rays (GCRs), as fully ionized astroparticles, are modulated with solar activity (e.g., Usoskin, 2017) which is manifested in the modification of the energy spectra of these GCRs in the heliosphere with respect to the very local interstellar spectra (VLIS) at the heliospheric heliopause (HP). The solar modulation of GCRs changes significantly with their energy (rigidity), is highly spatial dependent and their intensity varies with different time scales, periodically usually on the longer time scales (e.g., Krainev et al., 2021; Stozhkov et al., 2022) and non-periodically on a variety of shorter time scales (e.g., Modzelewska et al., 2020; Koldobskiy et al., 2022). In the context of describing observational features and the theoretical foundation, see reviews by Quenby (1984); Heber (2013), Kóta (2013) and Potgieter (2013), a recent observational review by Rankin et al., (2022, and references therein) and a comprehensive overview of the theory as applicable to the heliosphere by Engelbrecht et al., (2022, and references therein).

* Corresponding author at: Centre for Space Research, North-West University, Private Bag x2046, 2745 Mmabatho, South Africa.
E-mail address: Donald.Ngobeni@nwu.ac.za (M.D. Ngobeni).

https://doi.org/10.1016/j.asr.2023.12.025
0273-1177/

The availability of precise and simultaneous measurements of the proton (p) to total Helium (He) ratio, (p/He), and the $^3He_2$ to $^4He_2$ ratio ($^3He_2/^4He_2$) by the AMS-02 detector from 2011 to 2017 at the same rigidity (Aguilar et al., 2018, 2019) and p/He measured by PAMELA between 2006 and 2014 at a matching rigidity (Marcelli et al., 2020, 2022), provide prevailing evidence of a dependence on the mass-to-charge ratio (A/Z) and the very local interstellar spectra (VLIS) over a solar cycle. These observations revealed that both p/He and $^3He_2/^4He_2$ are not constant over time at rigidities below $\sim$ 2 GV. In particular, it was shown for the current solar cycle that the ratios had decreased significantly from 2014, in the A $>$ 0 magnetic field polarity cycle, in response to the declining level of solar activity (Aguilar et al., 2019). Whereas above 2–3 GV both p/He and $^3He_2/^4He_2$ were found to be essentially unchanged thus far less dependent on the changing level of solar activity.

Recently, a report by Marcelli et al. (2022) indicated that the time dependence of p/He observed by PAMELA below $\sim$ 1.5 GV has a time trend that is different to that between $\sim$ 1.5 GV and $\sim$ 3 GV, with the former decreasing through the maximum solar activity period while the latter gradually increased from 2009 to reach a maximum at the end of 2013. Unfortunately, PAMELA observations of $^3He_2/^4He_2$ below $\sim$ 1.5 GV is not yet available to confirm whether these different time trends also exist for $^3He_2/^4He_2$ based on a simultaneous investigation for both p/He and $^3He_2/^4He_2$ at this rigidity; see Lenni et al. (2021) for a progress report. However, the availability of reliable numerical modelling makes it possible to investigate this interesting time dependence simultaneously. Such studies by Corti et al. (2019), Tomassetti et al. (2019) and Song et al. (2021) also reported on aspects of this time dependence. In a first of our modelling reports on this topic, Ngobeni et al. (2020) argued and illustrated that these different time trends are the consequences of the effects of different A/Z for these GCRs but combined with the slopes of the modulated spectra at the Earth based on their respective VLIS's, and not due to any fundamental differences between the modulation of GCR protons and Helium. However, it is not yet established, at least not quantitatively, as to what extent individual elements of the diffusion tensor contribute to this interplay to reproduce the observed time trends in p/He and $^3He_2/^4He_2$, and in general for GCRs with dissimilar A/Z. This is the main purpose of this paper.

The first objective is to demonstrate that this model reasonably reproduces both PAMELA and AMS-02 observational spectra and their features for GCR protons and Helium over a wide rigidity range. As such, the assumptions about the global heliosphere as well as the modulation parameters, including diffusion and drift coefficients, are being tested and vindicated. The second objective is to investigate quantitatively the relative importance of the role of the parallel, radial perpendicular and polar perpendicular diffusion coefficients as the essential elements of the modulation process, on the time dependences of p/He and $^3He_2/^4He_2$ below 3 GV from 2006 to 2017. The approach is to first reproduce with our three-dimensional (3D) numerical model the simultaneously observed AMS-02 galactic proton spectra (1.00 GV– 60.3 GV), $^3He_2$ spectra (1.92 GV-15.3 GV) and $^4He_2$ spectra (2.15 GV-21.10 GV) for six periods including Bartels Rotations (BRs) 2433 (20 November-16 December 2011; 2011e), 2447 (02–28 December 2012; 2012e), 2460 (18 November-14 December 2013; 2013e), 2474 (01–27 December 2014; 2014e), 2487 (17 November-13 December 2015; 2015e) and 2501 (29 November – 25 December 2016; 2016e) together with PAMELA proton spectra (0.4 GV-47.0 GV) for three periods including Carrington Rotations 2117 (16 November-13 December 2011; 2011e), 2131 (02–29 December 2012; 2012e) and 2144 (21 November-12 December 2013; 2013e).

These modulated spectra over the mentioned period of time computed for a wide range of rigidity are then used to calculate p/He and $^3He_2/^4He_2$ for specific rigidity values. These values are compared with the corresponding observed trends in time of $^3He_2/^4He_2$ and p/He. In what follows we discuss the essence of the numerical model, assumptions made and the simulation approach, with focus on what is assumed for the three diffusion coefficients and the drift coefficient over time (solar activity). Results are presented first for proton, He-3 and He-4 spectra for the mentioned period then followed by the corresponding flux ratios. An interpretation of the main cause of the observed time trends in these ratios is given as a final result on which our conclusions are based.

2. Numerical model and simulation approach

This particular numerical approach and 3D model had been utilized extensively before, beginning with the interpretation of PAMELA observations of protons by Potgieter et al. (2014) and Vos and Potgieter (2015), PAMELA electrons by Potgieter et al. (2015), global GCR intensity gradients by Vos and Potgieter (2015), charge-sign dependent modulation by Potgieter and Vos (2017), Di Felice et al. (2017) and Aslam et al., (2021, 2023a,b), positron modulation by Aslam et al. (2019) and on establishing VLIS for various GCRs by Bisschoff et al. (2019). The same model was applied by Krainev et al. (2021) to describe features of long-term modulation over 22 years and used by Martucci et al. (2023) to interpret their proton observations in the ~50–250 MeV range. Simulations of GCR protons and Helium in particular are reported by Ngobeni et al., (2020, 2021) of which this report is a continuation. For reviews of this approach and results, see Potgieter (2014, 2017) and Potgieter et al. (2021). In what follows, we repeat only essential

assumptions of the basic features and parameters of the model concerning the aim and purpose of this work.

2.1. The basic features of the model

The transport equation (TPE) derived by Parker (1965) is solved numerically following the modelling approach of Potgieter et al., (2014, 2015). This TPE is

$$(\mathbf{V} + \langle \boldsymbol{v}_D \rangle).\nabla f - \nabla.(\boldsymbol{K}_s.\nabla f) - \frac{1}{3}(\nabla.\mathbf{V})\frac{\partial f}{\partial \ln p} = 0 \quad (1)$$

where f ($\boldsymbol{r}$, p, t) is the omnidirectional GCR distribution function, p is particle momentum, $\boldsymbol{r}$ is the heliocentric position vector, and t is time. The terms on the left-hand side represent convection caused by the expanding solar wind velocity $\mathbf{V}(r,\theta) = V(r,\theta)\boldsymbol{e}_r$, particle drifts caused by the gradients and curvatures of the heliospheric magnetic field (HMF) and its wavy heliospheric current sheet (HCS), particle diffusion, and adiabatic energy loss when $\nabla.\mathbf{V} > 0$. The latter process becomes dominant in the inner heliosphere at lower rigidity in the case of modulated spectra for protons and all GCR isotopes; see illustrations of this process by Moraal and Potgieter (1982). When this TPE is written in heliocentric spherical coordinate system, the coordinates r, θ, and ϕ represent radial distance, polar and azimuth angles, respectively. According to this system, the Earth is located at 1 AU in the equatorial plane with $\theta = 90°$. The relationship between f and the GCR differential intensity I is: $I = p^2 f = P^2 f$, where P is the rigidity of these GCR particles. In this equation, $\boldsymbol{K}_S$ is the symmetric diffusion tensor, the elements of which will be given and discussed further below. The averaged guiding centre drift velocity for a near isotropic CR distribution is given by

$$\langle \boldsymbol{v}_D \rangle = \nabla \times (K_A \boldsymbol{e}_B) \quad (2)$$

with $\boldsymbol{e}_B = \boldsymbol{B} / B$, where B is the magnitude of the background HMF at a given position in the heliosphere. Here, K_A is the drift coefficient specified by the off-diagonal elements of the generalized propagation tensor $\boldsymbol{K}$, that describes gradient and curvature drifts in the large-scale HMF. A strict requirement is that the divergence of this drift velocity is zero everywhere in the simulated heliosphere.

We assume the HMF to have a basic Parkerian geometry in the equatorial plane but modified in the polar regions similar to the approach of Smith and Bieber (1991), with the strict requirement that the divergence of this magnetic field is zero everywhere in the heliosphere. The appropriate equations, reasons, and effects for modifying the Parker HMF are described in detail by Raath et al. (2016). This modification is required to explain the observed GCR intensity latitudinal gradients as described by Vos and Potgieter (2016).

The features of this heliospheric modulation model are summarized as follows: The HP is assumed to be spherical and located at 122 AU from the Sun based on what was observed by Voyager 1 and Voyager 2 (Stone et al., 2013, 2019). It was established previously through modelling by Ferreira et al. (2004), Langner and Potgieter (2005a,b), and Ngobeni and Potgieter (2011) that the effects of a non-spherical HP on GCRs at 1 AU is smoothed out to become negligible. Following Vos and Potgieter (2015, 2016), the termination shock (TS) position (Stone et al., 2013) is assumed to move inward and outward depending on the phase of the solar cycle (Richardson and Wang, 2011). This means the width of the inner heliosheath changes with solar activity to have an effect on the modulation of GCRs even at 1 AU; see also Manuel et al. (2015). Reacceleration of GCRs at the TS is neglected because the focus here is on GCRs with rigidity above 0.92 GV; for an appraisal of these effects on low rigidity GCRs, see Langner et al. (2006), Langner and Potgieter (2004, 2005a,b, 2008) and Ngobeni and Potgieter (2010). Modulation beyond the HP as described by Luo et al., (2015, 2016) is neglected for the rigidity range that we study here. The expression for the wavy HCS (Jokipii and Thomas, 1981; Kóta and Jokipii, 1983) as applied is described in detail by Raath et al. (2015); see also Kopp et al. (2021) and Mohlolo et al. (2022). In accordance with the latitudinal dependence of solar wind speed observed by Ulysses (McComas et al., 2002; Heber, 2013), the averaged V is assumed to be $\sim$ 430 km/s in the slow solar wind region and $\sim$ 750 km/s in the fast solar wind region during solar minimum conditions. Following the observations made by Ulysses (see the overview by Heber and Potgieter, 2006), this latitude dependence is assumed to subside with increasing solar activity as utilized in numerical modelling by Ferreira et al. (2004), Moeketsi et al. (2005) and Nndanganeni and Potgieter (2016). Expressions for the global solar wind speed profile that change from solar minimum to maximum are given by Potgieter et al. (2015) and Potgieter and Vos (2017); see their equations 12 and 5, respectively. Expressions for the above-mentioned global features are duplicated and/or adapted and used in numerical modelling of GCRs by Zhao et al. (2014), Corti et al. (2019), Boschini et al., (2019; and references therein), Shen et al., (2019, 2021), Wang et al. (2019), Fiandrini et al. (2021) and Song et al. (2021). As done for previous applications of this particular 3D model, we continue to assume a steady state so that the results can be compared directly with previous studies. The model is not suitable to study GCR transient events and modulation less than one solar rotation as explained by Aslam et al., (2019, 2021).

2.2. Diffusion and drift modulation

The parameters that are changed with time in the model as proxies for solar activity to obtain the GCR results simulated in this study are the observed magnitude of the HMF, B, at the Earth and its polarity change during solar maximum, and the tilt angle (α) of HCS adapted from Aslam et al., (2021; see their Fig. 3). An updated figure of these solar activity proxies will be shown in the next sec-

tion. Additionally, the values and rigidity dependence of the three elements of the diffusion tensor, as discussed below, and the value of K_A are changed according to the required reproduction of the GCR proton and Helium spectra as observed at the Earth.

The symmetric diffusion tensor $\boldsymbol{K}_S$ in the HMF aligned coordinates consists of a diffusion coefficient $K_{\|}$ that is parallel to the average HMF, a radial perpendicular diffusion coefficient $K_{\perp r}$ and a polar perpendicular diffusion coefficient $K_{\perp\theta}$. In this study this tensor is given by

$$\mathrm{K}_S = \begin{pmatrix} K_{\|} & 0 & 0 \\ 0 & K_{\perp\theta} & 0 \\ 0 & 0 & K_{\perp r} \end{pmatrix} = K_{\|} \begin{pmatrix} 1 & 0 & 0 \\ 0 & 0.02 f_{\perp\theta} \frac{D^{\perp}}{D^{\|}} & 0 \\ 0 & 0 & 0.02 \frac{D^{\perp}}{D^{\|}} \end{pmatrix} \tag{3}$$

with

$$K_{\|} = (K_{\|})_0 \beta \left(\frac{B_0}{B}\right) \left(\frac{P}{P_0}\right)^{c_1} D^{\|}(P) \tag{4}$$

where

$$D^{\|}(P) = \left[\frac{\left(\frac{P}{P_0}\right)^{c_3} + \left(\frac{P_k}{P_0}\right)^{c_3}}{1 + \left(\frac{P_k}{P_0}\right)^{c_3}}\right]^{\frac{c_{2\|} - c_1}{c_3}} \quad and \; D^{\perp}(P) = \left[\frac{\left(\frac{P}{P_0}\right)^{c_3} + \left(\frac{P_k}{P_0}\right)^{c_3}}{1 + \left(\frac{P_k}{P_0}\right)^{c_3}}\right]^{\frac{c_{2\perp} - c_1}{c_3}} \tag{5}$$

with $(K_{\|})_0$ a scaling constant in units of 10^{22} cm^2 s^{-1}, β is the ratio of the particle speed v to the speed of light c; $P_0 = 1$ GV, $B_0 = 1$ nT to keep the rest of this equation dimensionless; $P_k = 4.0$ GV is the rigidity at which the transition between the two power laws occurs and is assumed to have a fix value, as done before, for the period simulated here, as such a simplification which is not necessarily the case over a full solar cycle. The values of $c_{2\|}$ (or $c_{2\perp}$) and c_1 respectively give the time dependence of the rigidity slopes of the diffusion coefficients above and below P_k, while $c_3 = 2.5$ is kept constant and gives the smoothness of the transition in these slopes. The ratio $D^{\perp}$ / $D^{\|}$ is the quantity that changes the rigidity dependence of $K_{\perp\theta}$ and $K_{\perp r}$ with respect to that of $K_{\|}$, and the function $f_{\perp\theta}$ (θ) enhances $K_{\perp\theta}$ by a factor 6.0 towards the polar regions with respect to its value in the equatorial plane (e.g., Potgieter, 2000; Ferreira et al., 2004; Moeketsi et al., 2005; Nndanganeni and Potgieter, 2016).

The drift coefficient in this study, expressed as a function of a simple drift reduction factor that depends only on rigidity is given by

$$K_A = k_{A0} \frac{\beta P}{3B} \frac{(P/P_{A0})^2}{1 + (P/P_{A0})^2} \tag{6}$$

with $P_{A0} = 0.75$ GV the rigidity below which the drift coefficient is suppressed with respect to the weak scattering approach in order to reproduce the mentioned Ulysses observations; its value is kept unchanged. On the other hand, $k_{A0,}$ a dimensionless quantity, can be adjusted to change the level of particle drift in the heliosphere related to solar activity and may vary between 0 (no drift at all) and 1.0 (full weak scattering drift) over a solar cycle. See the detailed discussion by Ngobeni and Potgieter (2015). The time variation of K_A in Equation (6) is determined by that of B (as explained below) and how k_{A0} is adjusted empirically as required by reproducing the GCR proton spectra over the solar cycle. For an explicit display of these features, see Aslam et al., (2023a; their Fig. 9-11) who used the same model applied here. In the figures below, the mean free paths (MFP, λ) and drift scale instead of the diffusion and drift coefficients will be shown with the general relationship given as: $\lambda = 3K/v = 3(K/\beta c)$.

2.3. Time-variations and procedure

The tilt angle α of the HCS and the magnitude B of the HMF at the Earth are changed from 2006 to 2017 as indicated in Fig. 1. The top panel shows the observed magnitude of the HMF at the Earth for this period taken from https://omniweb.gsfc.nasa.gov. Shaded parts indicate the period of no well-defined HMF polarity during solar maximum when the HMF changed from the A < 0 to A > 0 HMF polarity cycles as adapted from Aslam et al., (2021, 2023a,b), who discussed this aspect in great detail. Also shown in this panel is the corresponding ∼ 10 months (2006 to 2010) and ∼ 15 month (2011—2017) moving average of the HMF, as used in the model, indicated as blue open circles. In the bottom panel α at the Earth is shown for the same period taken from https://wso.stanford.edu. The corresponding calculated ∼15 months moving average values of α used in the model are shown as green open circles. The justification for these assumed averages is explained and discussed in detail by Aslam et al., (2019, 2021) as related to how long it takes for solar activity to propagate from the Sun to the HP (see also Vos and Potgieter, 2016). Because GCRs observed at the Earth depends on what solar activity is present in the global heliosphere at that time, it is to be expected that because of this averaging the model may sometimes over or under predict observations with time, especially when the tilt angle and/or magnetic field changes rapidly. This is not a concern because we are interested and focused on explaining the observed trends in time.

The changes in B and α are essential time varying input variables serving as proxies for solar activity for the modelling done in this study. Evidently, the value of B enters in the above equations to provide observationally motivated changes over time. Assuming all three diffusion coefficients to scale spatially as B_0/B is based on a simplified diffusion/-turbulence theory; for a more sophisticated approach, see e.g., Moloto et al. (2018) and for an overview of this theory, which is a work in progress, see Engelbrecht et al. (2022). These sophistications introduce additional variables

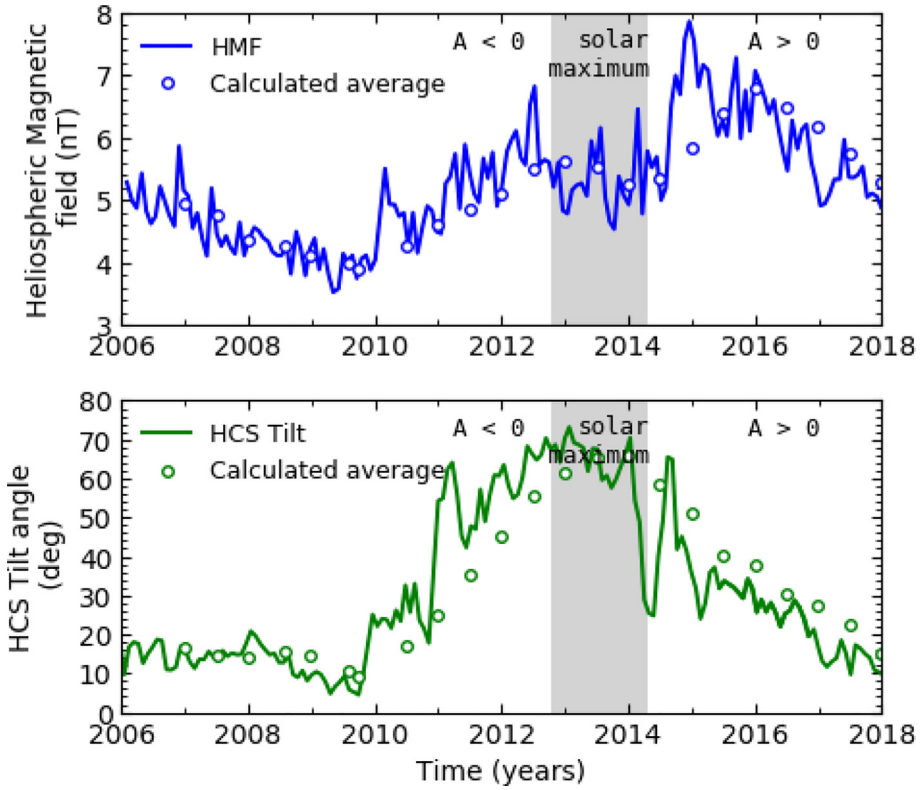

Fig. 1. Top panel: Magnitude B of the HMF (blue line) observed at the Earth averaged over Bartels Rotations (BRs) from 2006 to 2018 taken from http://omniweb.gsfc.nasa.gov; the corresponding running average values of B used in the model are indicated as open circles. Bottom panel: Carrington Rotation (CR) averages of the tilt angle α of the HCS (green line) at the Earth, for the same period, taken from http://wso.stanford.edu. Running average values of α used in the model are indicated as open circles. Shaded parts indicate the period of no well-defined HMF polarity during solar maximum when the HMF changed from $A < 0$ to $A > 0$ adapted from Aslam et al. (2022, 2023a,b). In this context, see also Sun et a. (2015).

related to the terminology used in turbulence theory, such as correlation lengths, and in order to establish their solar activity dependence, measurements of $\Delta B/B$ is required in the heliosphere; see e.g., Zhao et al. (2017). It has become evident that the conclusions about solar modulation of GCRs utilizing these sophistications in numerical models are qualitatively similar to what we have reported for our simplified approach. This is not surprising given that most of these studies are dedicated to explaining and reproducing GCR measurements; see e.g., the results of Shen et al. (2021).

Concerning the numerical method of solving the TPE, Aslam et al., (2023a) explained and discussed the application of the Alternating Direct Implicit (ADI) method (see also Potgieter and Moraal, 1985) is not unconditionally stable when a fifth numerical dimension is incorporated (that is, three spatial, one for rigidity/energy dependence, and one for time dependence). If all three spatial dimensions are used, the time dependence must be sacrificed. Numerous 2D time-dependent modeling results based on this ADI numerical scheme, when sacrificing the azimuthal dependence, had been published over the years e.g., le Roux & Potgieter (1992). The only alternative for a 3D approach with a full time-dependence is to use numerical models based on Stochastic Differential Equations (SDEs) which is a totally different approach to modulation studies, see e.g., Kopp et al. (2012), Bobik et al. (2016), Luo et al. (2019), Song et al. (2021) and Shen et al. (2021), and references therein. The SDE approach requires a sophisticated statistical procedure to decide when to stop the simulation of pseudo-particle trajectories for a given rigidity and location inside the heliosphere. In contrast, the ADI approach provides a full rigidity spectrum as a single solution and simultaneously for a given time everywhere in the heliosphere and for every type of GCR particles, which then can be used to calculate GCR intensity gradients and intensity ratios of these particles. Repeating this with time as solar activity changes provides spectra averaged for each solar rotation and over a solar cycle. Comparing these simulated spectra with observations over the same time span, conclusions can be obtained about how the physics contained in Parker's TPE is changing with the solar cycle. The GCR modeling done using the SDE approach has so far consistently confirmed the original predictions and results of ADI-type models, with the results of Shen et al. (2021) a prime example; see also Strauss and Potgieter (2014a, b); Raath et al. (2015) and Raath et al. (2016). The time variations reported here reflect how the propagation of GCRs has changed over this simulated period and is as

such a manifestation of the effects of the global modulation processes.

Concerning Eqs. (4) and (6), it follows that $(K_{\|})_0$, c_1 and $c_{2\|}$ (or $c_{2\perp}$) are related to the diffusion process and its rigidity dependence while k_{A0} relates to the drift process, and that they are assumed to change with time in addition to the observed time-dependence introduced through B and α as shown in Fig. 1. They are adapted from Ngobeni et al., (2020, 2022) as required by comparison of simulated proton spectra with available observations. The exact same set of modulation parameters to reproduce long-term time variation for proton spectra are then used to calculate corresponding spectra for the two Helium isotopes. This is a strict theoretical requirement because there is no support for any fundamental difference between the modulation of protons and these GCR isotopes. This assures that the essential modulation parameters are not changed in an ad-hoc and inconsistent manner for the purpose of producing best-fit parameter sets only applicable to observational data sets at the Earth. Furthermore, as mentioned above, complete spectra for protons, $^3He_2$ and $^4He_2$ are computed over a wide range of rigidity (kinetic energy) for every chosen BR, as will be illustrated below. These spectra are then used to calculate flux values at required rigidity bins to compare to available GCR observations, with p/He and ^{3}-$He_2/^4He_2$ ratios calculated afterwards.

Recently, similar numerical studies were reported of proton modulation by Fiandrini et al. (2021) and including GCR Helium by Song et al. (2021), focusing on AMS-02 observations. Tomassetti et al. (2019) simulated proton and Helium observations from AMS-02 and PAMELA. Wang et al. (2019) simulated several GCR species using a two-dimensional model. Shen and Qin (2018) simulated various sets of space observations over a range of energies, whereas Shen et al. (2021) focussed on Ulysses proton observations. All these numerical modeling studies share the common purpose of improving our understanding of the modulation processes over solar cycles, at least qualitatively, and in most cases particularly motivated by recent GCR observations at the Earth. However, it should be noted that when numerical modelling studies are done utilizing as measures of validation observation data over a limited range of rigidity and at only one location in the global heliosphere, such as at Earth, and neglecting other GCR observations beyond 1 AU, e.g., from Ulysses (Heber, 2013) and the two Voyager spacecraft (Rankin et al., 2022), these numerical modulation results and statistical based optimization of variables/parameters cannot be considered as generally applicable. Although we focus on AMS-02 observations at the Earth, our model contains all the necessary features to explain GCR observations of relevance as the list of references to our simulation testifies. An additional drawback of AMS-02 observations is that GCRs are reported only above 1 GV whereas large and spectacular modulation features occur below this rigidity as will be shown in Fig. 4 below.

3. Simulated results

It is illustrated by Ngobeni et al., (2020, 2022), that in order to reproduce the time trends in the observed proton, $^3He_2$ and $^4He_2$ spectra from PAMELA and AMS-02, the three diffusion coefficients and the drift coefficient in the model had to change over time from 2006 to 2017 as discussed above but not necessarily with the exact same amount at all rigidities. These established changes in time and incorporated into the model are shown in Fig. 2 with the three MFPs and drift scale normalized relative to 2006e. Clearly noted is that the change of particle drift (drift scale) is significant over this time period, reducing to small values during solar maximum activity when the HMF changes its polarity, with the rate of change during the descending phase before the reversal somewhat different from the ascending phase after the reversal. This is consistent to what Aslam et al., (2023a) reported when studying charge-sign-dependence for protons, electrons, and positrons. Evidently, the three diffusive MFPs also change with time but maintain the same relative changes at 1 GV, in fact at all rigidities below $P_k = 4$ GV. It remains to be established what specific modulation features arise when these MFPs do not maintain the same relative changes at lower rigidities where the observed ratios, p/He and $^3He_2/^4He_2$, indicate significant time dependences. This figure illustrates also qualitatively how solar modulation in the model has developed with time relative to 2006e, and how it changes from before to after the HMF polarity reversal period (Sun et al., 2015) during solar maximum activity. The details of how these elements change is further discussed and shown below with emphasis on the simulated (computed) time dependence of p/He and $^3He_2/^4He_2$.

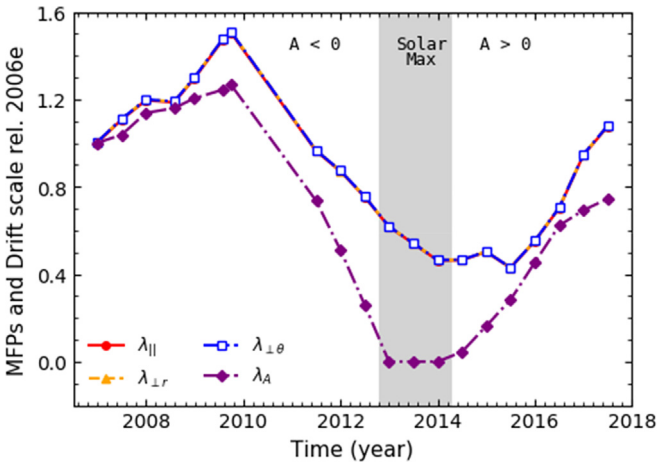

Fig. 2. Normalized three MFPs ($\lambda_{\|}, \lambda_{\perp r}, \lambda_{\perp\theta}$) and drift scale ($\lambda_A$) at the Earth for 1 GV protons and Helium as a function of time relative to the CR at the end of 2006 (14 November – 12 December 2006; 2006e) as they change for the A < 0 to the A > 0 HMF polarity epoch, respectively before and afterward the period of maximum solar activity when no well-defined HMF polarity was present (shaded band from Fig. 1).

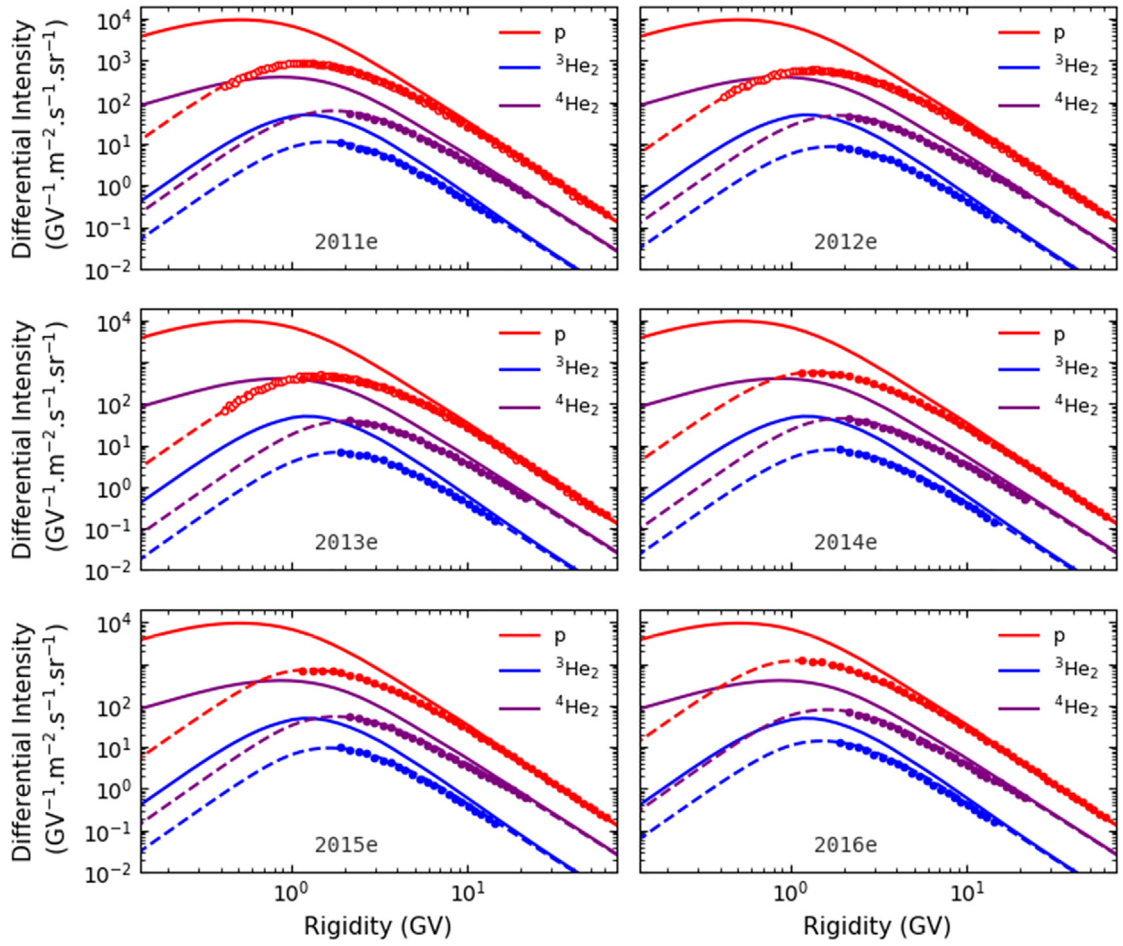

Fig. 3. Modulated proton (red dashed lines), $^3He_2$ (blue dashed lines) and $^4He_2$ (purple dashed lines) spectra, with respect to their individual VLIS's (coloured solid lines), computed as a function of rigidity, shown at the Earth for six periods between 2011e and 2016e. These modulated spectra are compared to the corresponding AMS-02 (coloured filled circles) and PAMELA observations (open red circles) reported by Aguilar et al. (2019) and Martucci et al. (2018), respectively.

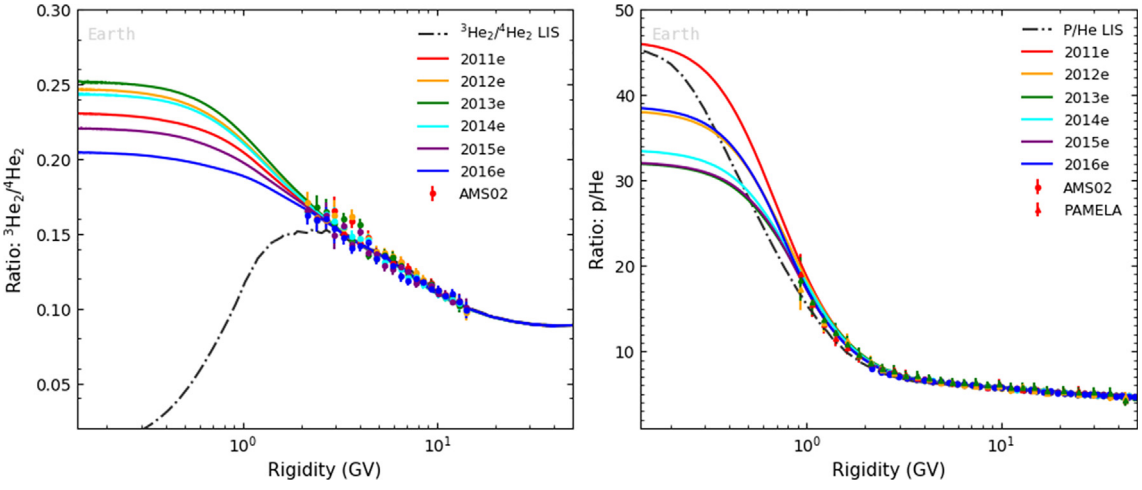

Fig. 4. The computed $^3He_2/^4He_2$ (left panel) and p/He ratios (right panel) as a function of rigidity for six periods between 2011e and 2016e are compared with AMS-02 and PAMELA observations taken at the same periods, from Aguilar et al. (2019) and Marcelli et al. (2022) respectively. Computed and observed ratios (with uncertainties depicted by error-bars) are represented by the coloured solid lines and symbols, respectively. As a reference the corresponding ratio of the VLIS's (at 122 AU) are given by dash-dotted dark grey lines in each panel.

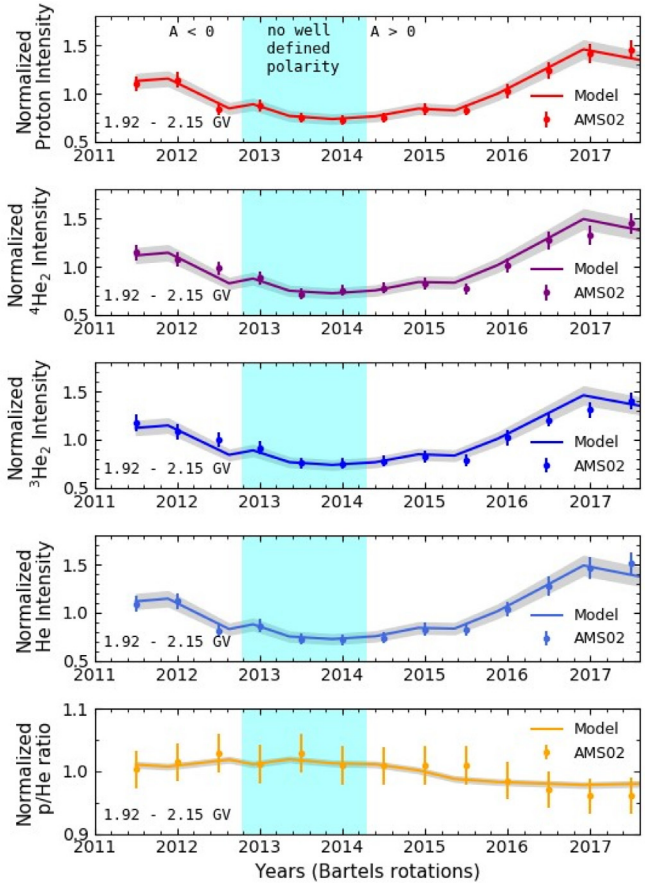

Fig. 5. Normalized simulated proton (red line), $^4He_2$ (purple line), $^3He_2$ (blue line) and total He (royalblue line) GCR intensity, together with the corresponding normalized p/He ratio (orange line) as a function of time for the period 2011 May to 2017 May (BRs 2426 to 2506) for rigidity range 1.92 – 2.15 GV. The normalization is done based on the average value for the period 2011 May to 2017 May. The grey shaded bands along and around the modeling results (all solid lines) indicate the standard error of the mean ($s/\sqrt{n}$). These normalized intensities are compared to the corresponding AMS02 (coloured filled circles) observations reported by Aguilar et al., (2019,2022). The cyan shaded regions indicate the period when there was no well-defined magnetic polarity during maximum solar activity (similar to grey regions in Fig. 1).

3.1. Spectra of p, $^3He_2$ and $^4He_2$ and the corresponding ratios

Reliable spectral shapes and values of the VLIS's of GCRs are of central importance in the general understanding of their global and total modulation in the heliosphere. These VLIS's are always assumed to provide the input spectra in numerical models to be modulated from a specified HP position up to the Earth (1 AU). In this paper, the VLIS used for protons is described in detail by Bisschoff et al. (2019), which is based on GALPROP model computations (see Moskalenko et al., 2002). This VLIS gives compatibility to both Voyager 1 (Stone et al., 2013; Cummings et al., 2016) and PAMELA (Adriani et al., 2013; Martucci et al., 2018) observations at low and high kinetic energies, respectively. The VLIS for He is derived by combining the GALPROP computed VLIS's for $^3He_2$ and $^4He_2$, modestly adjusted at higher rigidity according to AMS-02 observations for $^3He_2/^4He_2$ (Ngobeni et al., 2022). See the review on VLIS's by Potgieter et al. (2021) and references therein.

Fig. 3 depicts the computed galactic proton, $^3He_2$ and $^4He_2$ modulated spectra (dashed lines) with respect to their individual VLIS's (solid lines), specified at the HP (122 AU), as a function of rigidity in comparison with the corresponding observed AMS-02 spectra, along with PAMELA spectra, at the Earth. The difference between the modulated spectra at 1 AU and their respective VLIS at 122 AU illustrates the predicted total modulation of these particles as a function of rigidity. Note how the slopes of all the modulated spectra become similar at low rigidity as adiabatic energy losses becomes dominant and this happens for all A/Z values. Because of this process, the predicted total modulation at these low rigidities is evidently significant, being the largest for protons. Apart from the large difference in intensity levels, the slopes of the VLIS's for p, $^3He_2$ and $^4He_2$ are significantly different at rigidities below $\sim$ 1.5 GV, also having spectral peaks at different rigidity values. The modulation process changes the slopes of the VLIS's at all rigidities as the intensity levels decrease, evidently less at high rigidity than at low rigidity where the effect becomes significant. This process causes the peak intensity values of the modulated spectra to shift consistently to higher rigidity compared to their VLIS values, as discussed at great length by Ngobeni et al., (2020; see their Figure 13). This emphasizes the prominent features of the modulated spectra at the Earth for species with different VLIS's and A/Z.

The essence of Fig. 3 is to show that when using the same set of modulation parameters, the observed spectra for Galactic protons, $^3He_2$ and $^4He_2$ from AMS-02, together with PAMELA proton spectra, taken at matching periods between 2011 and 2017, are simultaneously and reasonably reproduced by the numerical model. Simulation of the new result on the time variation of protons from AMS-02 (Aguilar et al., 2021), based on this exact same model, has been done by Aslam et al., (2023b; see their Fig. 3) over a wide range of rigidity values. The clearly distinguishable modulation effects of $^3He_2$ and $^4He_2$ as depicted in this figure can explicitly be utilized to simulate quantitatively the time trends in p/He and $^3He_2/^4He_2$ below $\sim$ 3 GV between 2006 and 2017. As a first step, we need to illustrate how these ratios changed as a function of rigidity between 2011e and 2016e.

The computed $^3He_2/^4He_2$ for this period as a function of rigidity with respect to their corresponding VLIS's, are shown in the left panel of Fig. 4 and compared with AMS-02 observations. The objective of this figure is to illustrate in the first place how large the modulation effects become with decreasing rigidity, starting below 1–2 GV, and how it changes with solar activity. For a comparison of this computed ratio with a large number of other observations, see also Ngobeni et al., (2022; their Fig. 4). Below this value the computed ratios begin to differ significantly and progressively in time, from a maximum value during

solar maximum conditions as represented by 2013e. In terms of decreasing rigidity, they still increase below ~ 2 GV but with different slopes depending on the chosen time period, until they start to level off consistently to reach eventually unchanged values at the lower rigidity range. This, of course, is because of the adiabatic energy losses dominating the shape of the modulated spectra as shown in Fig. 3. Because of this dominant effect, the modulated ratios at Earth evidently do not follow the rigidity dependence of the ratio of the VLIS's (at 122 AU) below 2–3 GV, again consistent to what is shown in Fig. 3. In contrast, above this rigidity the modulation effects become progressively less but not negligible as the spread in observational values are noticeable. It follows that the simulated solutions are all within the observational boundaries for this ratio so that we consider them adequately reproduced by our model. What is worth mentioning as pointed out by Ngobeni et al. (2021), is that an apparent power law rigidity dependence is exhibited for how this ratio behave above ~ 3 GV and with time. The index of this power law is different from that of the VLIS ratios and changes with solar activity. This nice power law behaviour is obviously dissipating with decreasing rigidity when the modulation process is being influenced progressively by the other mechanisms such as particle drift and adiabatic energy loss as mentioned above. See Figs. 6 and 7 by Potgieter and Vos (2017) on how this model predicts drift effects to increase significantly with decreasing rigidity for protons to overshadow diffusion effects until the adiabatic energy loss effects are taking over as the dominant modulation mechanism.

Similarly, the right panel of Fig. 4 shows the computed p/He and those observed from AMS-02 and PAMELA as a function of rigidity also between 2011e and 2016e. The spread of these observational values, with He now taken as the sum of He-3 and He-4, are evidently less than when He-3 and He-4 are compared. Overall, the value and shape of p/He are well reproduced with the numerical model with the rigidity dependence of the ratio of the modulated spectra tracking the rigidity slope of the corresponding VLIS ratio with P >~5 GV and with changing modulation conditions. This may be interpreted to signify that the observed p/He by AMS-02 and PAMELA above ~ 5 GV essentially, but not exactly, reveals the difference in the rigidity dependence of the VLIS's for protons and He, providing evidence about the difference in their origin and propagation in the interstellar medium. Obviously, the higher the rigidity and the less the modulation becomes, the more exact this becomes. However, with decreasing rigidity solar modulation causes it to deviate progressively

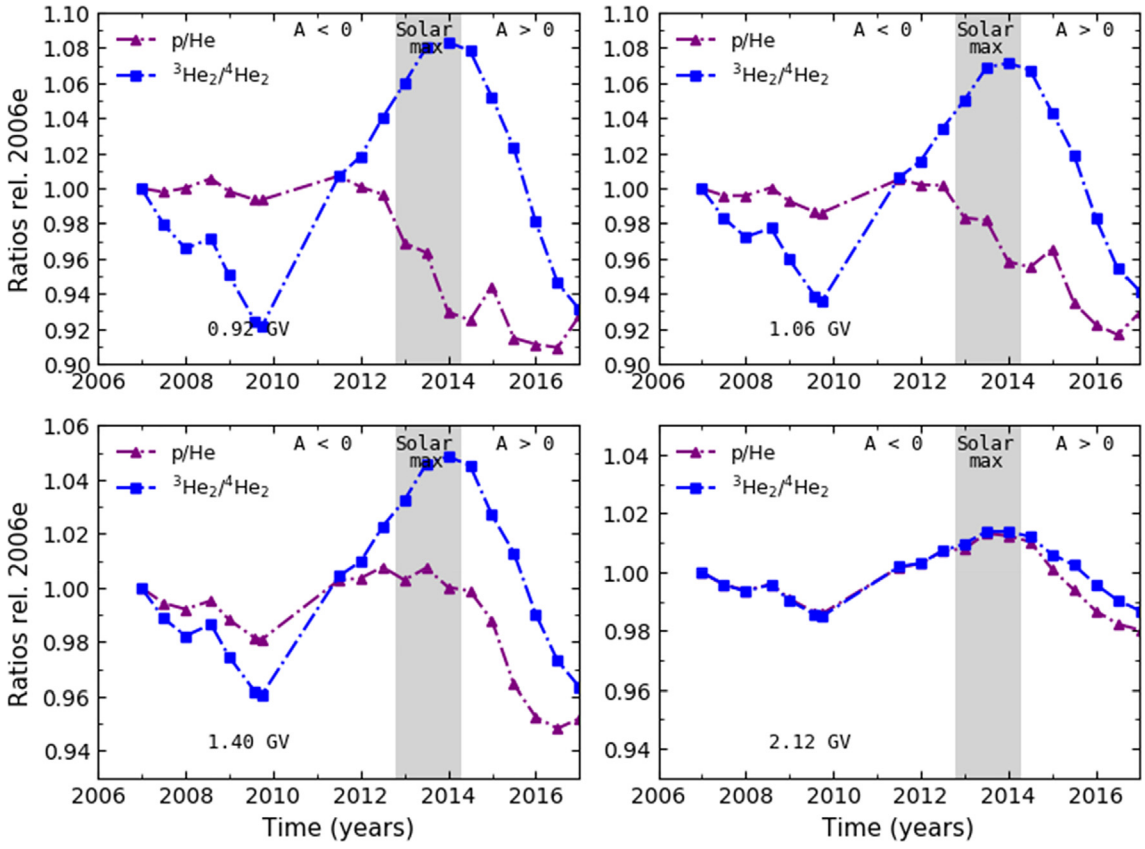

Fig. 6. Computed p/He (purple lines) and $^3He_2/^4He_2$ (blue lines) as a function of time, normalized with respect to 2006e, at the Earth for four rigidity values between 0.92 GV and 2.12 GV. The grey shaded regions indicate the period when there was no well-defined magnetic polarity during maximum solar activity.

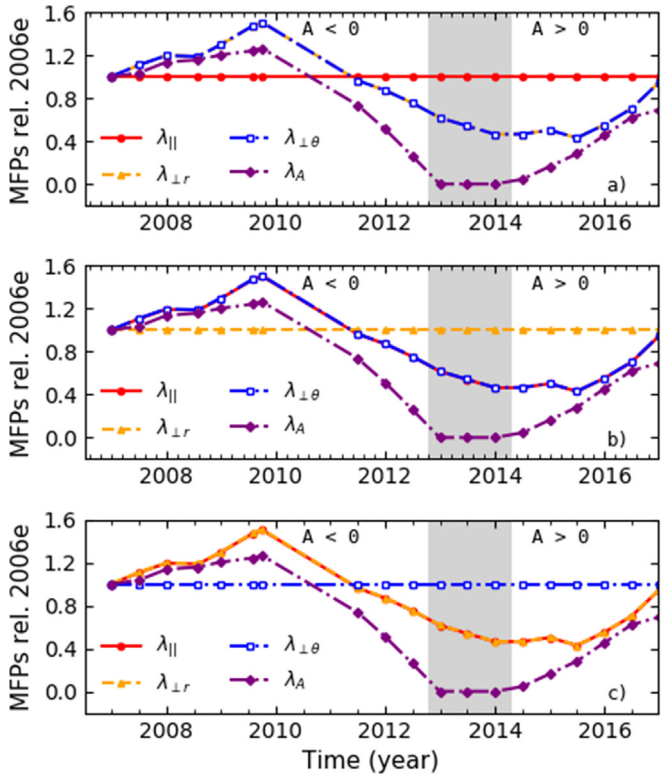

Fig. 7. Three scenarios of the time dependence of the MFPs and drift scale, in units of AU, shown here at the Earth for a rigidity of 1 GV. In panels a), b) and c), $\lambda_{||}$ (red), $\lambda_{\perp r}$ (orange), $\lambda_{\perp\theta}$ (blue), respectively, are kept unchanged relative to 2006e while other modulation parameters and conditions are changing as in Figs. 1 and 2.

from these values. These aspects are discussed in detail by Ngobeni et al. (2020). Comparing how the slopes in the ratios differ with time and with decreasing rigidity in the lower ranges where adiabatic energy losses become dominant, the p/He is quantitatively different from $^3He_2/^4He_2$ although the same qualitative features remain. Again, this relates directly to what is shown in Fig. 3. These interesting qualitative time trends in both p/He and $^3He_2/^4He_2$ is further explored in the next figures.

To better assess the long-term time variation of the simultaneously observed AMS02 proton, $^3He_2$, $^4He_2$, total He intensities and the proton-to-helium ratios at the exact same rigidity bin from May 2011 to May 2017, Fig. 5 shows their normalized simulated intensities compared with normalized AMS02 observations over the same period. The corresponding normalized p/He ratio is shown in the bottom panel. The normalization is done with respect to average value for the period 2011 May to 2017 May and provides a common reference level for comparison of the time trend produced by the model and observations, and what it takes from a physics point of view to simultaneously reproduce these long-term time variations for species with different VLIS and A/Z. The comparison in this figure establishes that the simulated intensities of proton, $^3He_2$, $^4He_2$, total He and their corresponding p/He ratio exhibit similar long-term time trends with AMS02 observation between 2011 and 2017. Therefore, the relative importance of the role of the elements of the diffusion tensor on the long-term time trends of p/He and $^3He_2/^4He_2$ below 3 GV from 2006 to 2017 can be investigated.

In the context of comparing simulations to observations, the AMS-02 measurements above $\sim$ 2 GV are central to study the time variation of $^3He_2/^4He_2$ (Ngobeni et al., 2022). However, below $\sim$ 2 GV, PAMELA observations, as all other observations with a lower rigidity thresh-hold, are well suited to study the much larger time dependence in $^3He_2/^4He_2$. In what follows we refrain from making any further direct comparisons between our simulations and observations, focussing instead on the time trends produced for these ratios by the model. Fig. 6 displays the time variation in p/He and $^3He_2/^4He_2$ relative to 2006e to highlight the time trends and differences in these ratios between 2006 and 2017. Evidently, the time variation of p/He below 1.5 GV is significantly different from 2.12 GV; at this low rigidity values p/He decreases through the solar maximum activity period, whereas at rigidities 2.12 GV the trend is opposite. This behaviour of p/He has been reported for PAMELA observations (Marcelli et al., 2022). In the A $<$ 0 cycle the computed time trend in p/He below $\sim$ 1 GV is not changing significantly before the solar maximum period but decreases noticeably in the A $>$ 0 cycle after the solar maximum conditions. In contrast, the computed $^3He_2/^4He_2$ ratios show almost identical time dependences below $\sim$ 3 GV, systematically decreasing and increasing with solar activity to reach maximum values during solar maximum conditions. These different trends of the p/He and $^3He_2/^4He_2$ below $\sim$ 1.5 GV are mainly caused by the rigidity slopes of the diffusion coefficients that change differently before solar maximum than afterwards, and that this influences the modulation of GCRs nuclei with dissimilar VLIS's and A/Z values somewhat differently, which is consistent to the report by Ngobeni et al. (2022).

Determining which of the three elements of the diffusion tensor plays a dominant role in shaping these time trends in the mentioned ratios is the focus of what follows next. It is done by performing illustrative numerical modelling exercises (simulation scenarios).

3.2. Implications for the time dependence of elements of the diffusion tensor

To provide the context of using a numerical exercise for investigating the relative roles of the time dependence of the three MFPs related to the time variation of p/He and $^3He_2/^4He_2$ below 3 GV, they are kept unchanged one after another, each with time relative to 2006e. This is shown in Fig. 7, first for $\lambda_{||}$ (or 3 $K_{||}/\beta/c$) (panel a), then $\lambda_{\perp r}$ (panel b) and $\lambda_{\perp\theta}$ (panel c), respectively. This way, the rigidity slope of the respective MFP is not changed at all with time, while the other modulation conditions and parameters, as well as drift scale, are scaled with time as in Fig. 2. These

simulations will be used to illustrate in terms of the relevant physics intrinsic to the numerical model, how the relation between the considered scenarios of time changes in the MFPs influence the trends in the behaviour of p/He and $^3He_2/^4He_2$. This will further clarify which of the three elements of the diffusion tensor plays a dominant role in shaping these time trends, especially before and after solar maximum activity periods.

In Fig. 8 the computed p/He ratios are shown at four rigidities from 2006 and 2017. Each of the four panels represents solutions obtained from the corresponding three scenarios of MFPs given in Fig. 7 and the reference model with the complete time dependence shown in Fig. 2. Here, the effects on the computed p/He of neglecting the time dependence of one of the individual diffusion coefficients are illustrated with emphasis on the resulting differences between these restrictive solutions for each of the three scenarios of MFPs (coloured lines) and the one using the complete model (black solid line). A comparison illustrates that the contribution of the time dependence of $K_{\perp r}$ is a dominant cause of the observed time variation. This differs for the two polarity epochs; at all rigidities shown, p/He remains relatively unaffected in the A < 0 cycle in response to the assumed constant value in $K_{\perp r}$, whereas in the A > 0 it decreases noticeably after solar maximum conditions, but not nearly as noteworthy as that obtained with the complete model. It follows that with the omission of the time dependence of $K_{\perp r}$, both in value and rigidity slopes, the model produces trends in p/He that is not observed below 3 GV at the Earth. As seen in all four panels, the time and rigidity changes in $K_{\parallel}$ and $K_{\perp\theta}$ produce some small effects but this clearly plays a less significant role in shaping the behaviour of the time trends in p/He.

Fig. 9 is similar to Fig. 8 but now the effects on $^3He_2/^4He_2$ are illustrated over the same period and for the same rigidity values. It is readily seen that when the time dependence of $K_{\perp r}$ is neglected the effect on this ratio is also significant, with the differences decreasing systematically with increasing rigidity, with no clear maximum in the restricted ratios associated with maximum solar activity. In contrast to the trends in p/He in Fig. 8, these differences are also conspicuously less in the A > 0 cycle. Again, the time and rigidity changes in $K_{\parallel}$ and $K_{\perp\theta}$ also produce some small effects but notably less in shaping the behaviour of the time trends in $^3He_2/^4He_2$.

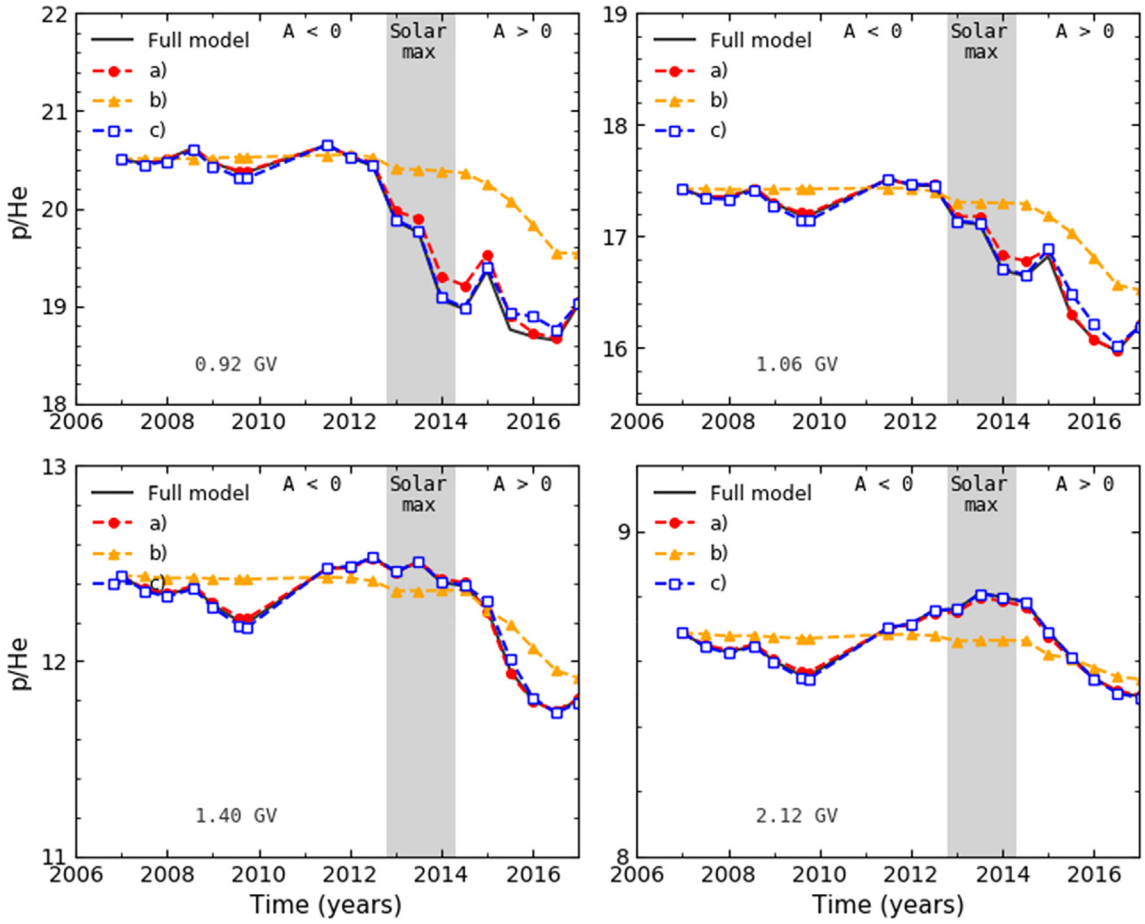

Fig. 8. The computed p/He ratios for four rigidities between 0.92 GV and 2.12 GV, as a function of time at Earth (1 AU in the equatorial plane) corresponding to the four illustrative scenarios of MFPs and drift scale shown in Figs. 2 and 7. Solutions obtained for the actual and complete time dependence shown in Fig. 2 are indicated by solid black lines, whereas coloured lines indicated as a), b) and c) represent solutions obtained according to assumptions made for the three respective scenarios (panels) shown in Fig. 7.

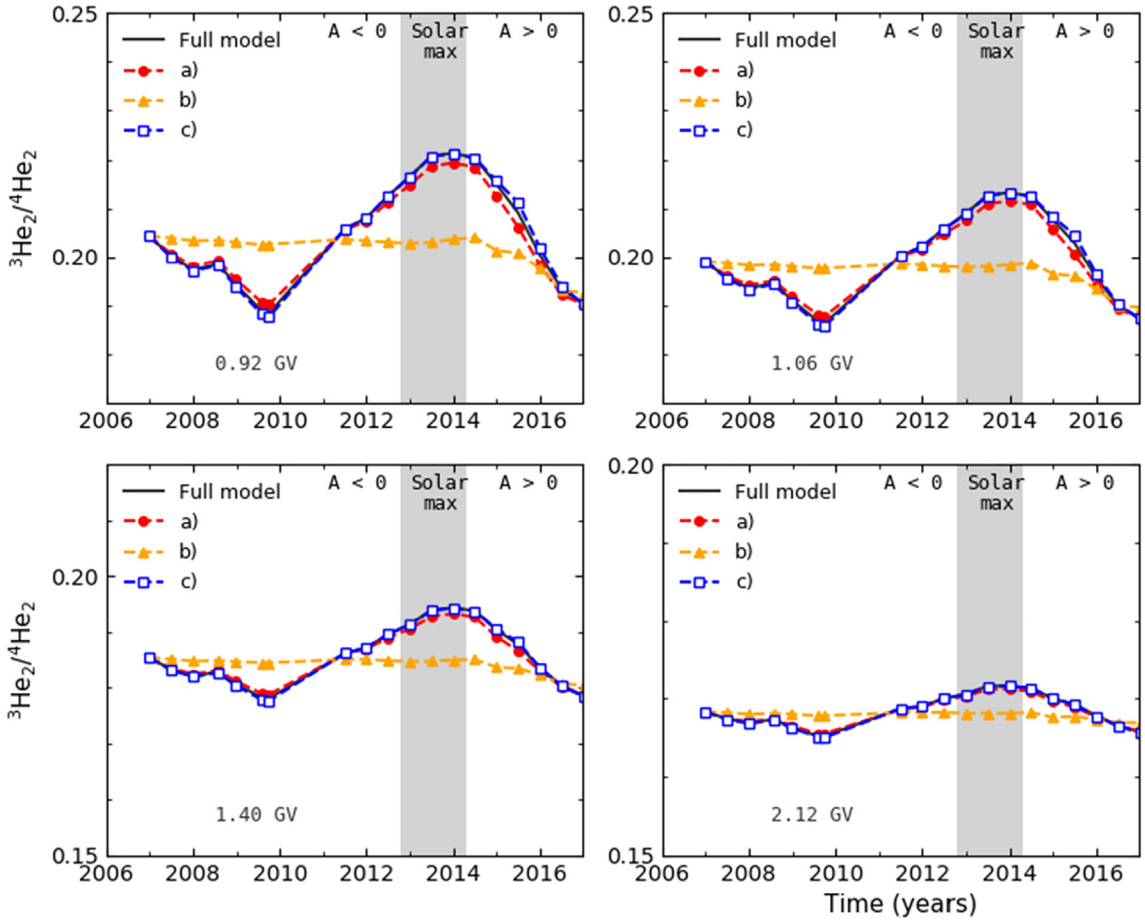

Fig. 9. . Similar to Fig. 8 but now shown for $^3He_2/^4He_2$.

4. Discussion, summary and conclusions

The main purpose of this work is to illustrate with a 3D numerical model the relative roles of the three diffusion coefficients on the time dependences of p/He and $^3He_2/^4He_2$ at rigidities between 1 and 3 GV, applicable to the period 2006 to the beginning of 2017. This includes the periods of minimum modulation in 2009 and maximum modulation from ~ 2012 to 2014. The exact same set of modeling and modulation parameters, diffusion and drift coefficients that reproduce proton spectra were also used to reproduce the two helium isotopes spectra as illustrated in Fig. 3, assuring that the modeling parameters are not changed in an ad-hoc and inconsistent manner for the purpose of simply fitting different observational data sets at the Earth. The known and motivated differences in the modulation of protons and the helium isotopes are their intrinsic A/Z-values and respective VLIS's, the latter illustrated comprehensively in Fig. 3.

The computed values for p/He and $^3He_2/^4He_2$ are shown over a wide range of rigidity in Fig. 4 and how these values change from 2011 to the end of 2016. They are compared to observed ratios from PAMELA and AMS-02 over the same period, illustrating that the model effectively reproduces the observational features. A conspicuous result is that down to ~ 3 GV, the modulated $^3He_2/^4He_2$ at the Earth follows the rigidity trend of the ratio of their respective VLIS's but below this rigidity it deviates substantially, in contrast to p/He. The role of adiabatic energy losses on these ratios at the Earth is also illustrated.

The time variations of the computed ratios relative to 2006e are shown explicitly in Fig. 6, between 0.92 GV and 2.12 GV. The modelling results signify how $^3He_2/^4He_2$ decreases towards solar minimum below ~ 2 GV, and that it is consistently larger than the time trends for p/He but the differences subside with increasing rigidity to dissipate at 2.12 GV. The p/He at 0.92 GV and 1.06 GV decreases over the solar maximum period, but this trend is clearly changed at 1.40 GV and 2.12 GV where a maximum in this ratio occurs at solar maximum; see also Marcelli et al. (2022). The latter trend is more like $^3He_2/^4He_2$ which shows a clear minimum value at solar minimum and a clear maximum at solar maximum modulation conditions at all four rigidity values. Evidently, a qualitative conclusion can be made that the time variations of p/He are different below 1.5 GV than above it.

The differences in time variation between p/He and $^3He_2/^4He_2$ below 1.5 GV occurs despite that the exact same modulation parameters are used for these GCRs (Fig. 2). This is mainly a consequence of adiabatic energy losses

which begin to dominate at higher rigidities for $^3He_2$ than for $^4He_2$, and for total Helium than for protons. Inspection shows that the slope of the $^3He_2$ VLIS is overall closer to the characteristic adiabatic energy slope (of kinetic energy, E^1) of the modulated spectrum (Fig. 3) than that of $^4He_2$ at lower rigidities. This contributes to the relative changes in the $^3He_2$ intensity in remaining less than for $^4He_2$ at rigidities below $\sim$ 3 GV with solar activity. Similar for Helium and protons, with the relative proton intensity varying more than for Helium with decreasing rigidity below $\sim$ 1 GV; for additional discussion, see also Ngobeni et al. (2020). This is further indicative of the important role of the differences in the shapes of their VLIS's below 3 GV, as an important insight from numerical modeling studies that is not possible to realize from observational studies alone.

The computed results illustrate that the contribution of the time dependence of $K_{\perp r}$ is the dominant cause of the observed time variation in p/He and $^3He_2/^4He_2$, in particular during the A $<$ 0 cycle. The effects of the time dependence of $K_{\parallel}$ and $K_{\perp\theta}$ on the time dependences of p/He and $^3He_2/^4He_2$ ratios at rigidities below 3 GV are far less notable, although not to be ignored. Our results stipulate that neglecting the time dependence of $K_{\perp r}$, both in value and rigidity, from numerical models would produce time trends for both p/He and $^3He_2/^4He_2$ that are incongruent with observed trends at the Earth. It is to be emphasized that the differences between the time trends of these ratios observed by AMS-02 (Aguilar et al., 2019) are not the cause of any fundamental difference between the solar modulation of galactic protons and Helium.

Declaration of competing interest

The authors declare that they have no known competing financial interests or personal relationships that could have appeared to influence the work reported in this paper.

Acknowledgements

MDN thanks the SA National Research Foundation (NRF) for partial financial support under Italy and SA Joint Research Programme (Grant no: 150556). He also acknowledges that the opinions, findings and conclusions or recommendations expressed in any publication generated by the NRF supported research is that of the authors alone, and that the NRF accepts no liability whatsoever in this regard. OPMA acknowledges the support from the Shandong Institute of Advanced Technology (SDIAT) and NSFC Project U2106201.

References

Adriani, O., Barbarino, G.C., Bazilevskaya, G.A., et al., 2013. Time dependence of the proton flux measured by PAMELA during the 2006 July-2009 December solar minimum. Astrophys. J. 765, 91.

Aguilar, M., Ali Cavasonza, L., Alpat, B., et al., 2018. Observation of fine time structures in the cosmic proton and helium fluxes with the alpha magnetic spectrometer on the International Space Station. Phys. Rev. Lett. 121, 051101.

Aguilar, M., Ali Cavasonza, L., Ambrosi, G., et al., 2019. Properties of Cosmic Helium Isotopes Measured by the Alpha Magnetic Spectrometer. Phys. Rev. Lett. 123, 181102.

Aguilar, M., Ali Cavasonza, L., Ambrosi, G., et al., 2022. Properties of Daily Helium Fluxes. Phys. Rev. Lett. 128, 231102.

Aslam, O.P.M., Bisschoff, D., Potgieter, M.S., Boezio, M., Munini, R., 2019. Modeling of Heliospheric Modulation of Cosmic-Ray Positrons in a Very Quiet Heliosphere. Astrophys. J. 873, 70.

Aslam, O.P.M., Bisschoff, D., Ngobeni, M.D., Potgieter, M.S., Munini, R., Boezio, M., Mikhailov, V.V., 2021. Time and Charge-sign Dependence of the Heliospheric Modulation of Cosmic Rays. Astrophys. J. 909, 215.

Aslam, O.P.M., Luo, X.i., Potgieter, M.S., Ngobeni, M.D., Song, X., 2023a. Unfolding Drift Effects for Cosmic Rays over the Period of the Sun's Magnetic Field Reversal. Astrophys. J. 947, 72.

Aslam, O.P.M., Potgieter, M.S., Luo, X.i., Ngobeni, M.D., 2023b. Modulation of Cosmic-Ray Antiprotons in the Heliosphere: Simulations for a Solar Cycle. Astrophys. J. 953, 101.

Bisschoff, D., Potgieter, M.S., Aslam, O.P.M., 2019. New very local interstellar spectra for electrons, positrons, protons, and light cosmic ray nuclei. Astrophys. Astrophys. J. 878, 59.

Bobik, P., Boschini, M.J., Della Torre, S., Gervasi, M., Grandi, D., La Vacca, G., Pensotti, S., Putis, M., Rancoita, P.G., Rozza, D., Tacconi, M., Zannoni, M., 2016. On the forward-backward-in-time approach for Monte Carlo solution of Parker's transport equation: One-dimensional case. J. Geophys. Res. 121, 3920.

Boschini, M.J., Della Torre, S., Gervasi, M., La Vacca, G., Rancoita, P. G., 2019. Deciphering the Local Interstellar Spectra of Secondary Nuclei with the Galprop/HelmodFramework and a Hint for Primary Lithium in Cosmic Rays. Adv. Space Res. 64, 2459.

Corti, C., Potgieter, M.S., Bindi, V., Consolandi, C., Light, C., Palermo, M., Popkow, A., 2019. Numerical modeling of galactic cosmic ray proton and helium observed by AMS-02 during the solar maximum of Solar Cycle 24. Astrophys. J. 871, 153.

Cummings, A.C., Stone, E.C., Heikkila, B.C., Lal, N., Webber, W.R., Jóhannesson, G., 2016. Galactic cosmic rays in the local interstellar medium: Voyager 1 observations and model results. Astrophys. J. 831, 18.

Di Felice, V., Munini, R., Vos, E.E., Potgieter, M.S., 2017. New evidence for charge-sign dependent modulation during the solar minimum of 2006 to 2009. Astrophys. J. 834, 89.

Engelbrecht, N.E., Effenberger, F., Florinski, V., Potgieter, M.S., Ruffolo, D., Chhiber, R., Usmanov, A.V., Rankin, J.S., Els, P.L., 2022. Cosmic ray transport theory in the heliosphere. Space Sci Rev. 218, 33.

Ferreira, S.E.S., Potgieter, M.S., Scherer, K., 2004. Modulation of Cosmic-Ray Electrons in a Nonspherical and Irregular Heliosphere. Astrophys. J. 607, 1014.

Fiandrini, E., Tomassetti, N., Bertucci, B., Donnini, F., Graziani, M., Khiali, B., 2021. Numerical modeling of cosmic rays in the heliosphere: Analysis of proton data from AMS-02 and PAMELA. Phys. Rev. D. 104, 023012.

Heber, B., 2013. Cosmic rays through the solar Hale Cycle. Insights from Ulysses. Space Sci. Rev. 176, 265.

Heber, B., Potgieter, M.S., 2006. Cosmic rays at high heliolatitudes. Space Sci. Rev. 127, 117.

Jokipii, J.R., Thomas, B., 1981. Effects of drift on the transport of cosmic rays IV. Modulation by a wavy interplanetary current sheet. Astrophys. J. 243, 1115.

Koldobskiy, S.A., Kähkönen, R., Hofer, B., Krivova, N.A., Kovaltsov, G.A., Usoskin, I.G., 2022. Time Lag Between Cosmic-Ray and Solar Variability: Sunspot Numbers and Open Solar Magnetic Flux. Solar Phys. 297, 38.

Kopp, A., Büsching, I., Strauss, R.D., Potgieter, M.S., 2012. A stochastic differential equation code for multidimensional Fokker-Planck type problems. Comp. Phys. Comm. 183, 530.
Kopp, A., Raath, J.L., Fichtner, H., Potgieter, M.S., Ferreira, S.E.S., Heber, B., 2021. Cosmic-Ray Transport in Heliospheric Magnetic Structures. III. Implications of Solar Magnetograms for the Drifts of Cosmic Rays. Astrophys. J. 922, 2.
Kóta, J., 2013. Theory and modeling of galactic cosmic rays: Trends and prospects. Space Sci. Rev. 176, 391.
Kóta, J., Jokipii, J.R., 1983. The effects of drifts on the transport of cosmic rays. VI. A three-dimensional model including diffusion. Astrophys. J. 265, 573.
Krainev, M., Kalinina, M., Aslam, O.P.M., Ngobeni, M.D., Potgieter, M. S., 2021. On the dependence of maximum GCR intensity on heliospheric factors for the last five sunspot minima. Adv. Space Res. 68, 2953.
Langner, U.W., Potgieter, M.S., 2004. Effects of the solar wind termination shock on charge-sign dependent cosmic ray modulation. Adv. Space Res. 34, 144.
Langner, U.W., Potgieter, M.S., 2005a. Effects of the solar wind termination shock and heliosheath on theheliospheric modulation of galactic and anomalous Helium. Ann. Geophys. 23, 1.
Langner, U.W., Potgieter, M.S., 2005b. The modulation of galactic protons in an asymmetrical heliosphere Astrophys. J. 630, 1114.
Langner, U.W., Potgieter, M.S., Fichtner, H., Borrmann, T., 2006. Effects of different solar wind speed profiles in the heliosheath on the modulation of cosmic-ray protons. Astrophys. J. 640, 1119.
Langner, U.W., Potgieter, M.S., 2008. The role of radial perpendicular diffusion and latitude dependent acceleration along the solar wind termination shock. Adv. Space Res. 41, 368.
le Roux, J.A., Potgieter, M.S., 1992. The simulated features of heliospheric cosmic ray modulation with a time-dependent drift model. II. On the energy dependence of the onset of new modulation in 1987. Astrophysical J. 390, 661.
Lenni, A., Boezio, M., Marcelli, N., Munini, R., Menn, W., Marcelli, N., Potgieter, M.S., et al., 2021. Study of the solar modulation for the cosmic ray isotopes with the PAMELA experiment. PoS (ICRC2021), 1310.
Luo, X., Zhang, M., Potgieter, M.S., Feng, X., Pogorelov, P., 2015. A numerical simulation of cosmic-ray modulation near the heliopause. Astrophysical J. 808 (82), 1.
Luo, X., Potgieter, M.S., Zhang, M., Pogorelov, N., Feng, X., Strauss, R. D., 2016. A numerical simulation of cosmic ray modulation near the heliopause. II. Some Physical Insights. Astrophysical J. 826, 182.
Luo, X., Potgieter, M.S., Zhang, M., Feng, X., 2019. A Numerical Study of Cosmic Proton Modulation Using AMS-02 Observations. Astrophys. J. 878, 6.
Manuel, R., Ferreira, S.E.S., Potgieter, M.S., 2015. The effect of a dynamic inner heliosheath thickness on cosmic-ray modulation. Astrophys. J. 799, 223.
Marcelli, N., Boezio, M., Lenni, A., Menn, W., Munini, R., Aslam, O.P. M., et al., 2020. Time dependence of the flux of Helium nuclei in cosmic rays measured by the PAMELA Experiment between 2006 July and 2009 December. Astrophys. J. 893, 145.
Marcelli, N., Boezio, M., Lenni, A., Menn, W., Munini, R., Aslam, O.P. M., et al., 2022. Helium Fluxes Measured by the PAMELA Experiment from the Minimum to the Maximum Solar Activity for Solar Cycle 24. Astrophys. J. Lett. 925, L24.
Martucci, M., Ammendola, R., Badoni, D., Bartocci, S., Battiston, R. et al. (HEPD-01 collaboration), 2023. Time Dependence of 50 – 250 MeV Galactic Cosmic-Ray Protons between Solar Cycles 24 and 25, Measured by the High-energy Particle Detector on board the CSES-01. Astrophys. J. Lett. 945, L39.
Martucci, M., Munini, R., Boezio, M., Di Felice, V., Adriani, O., Barbarino, G.C., et al., 2018. Proton fluxes measured by the PAMELA experiment from the minimum to the maximum solar activity for the 24th solar cycle. Astrophys. J. Lett. 854, L2.
McComas, D.J., Elliott, H.A., Gosling, J.T., et al., 2002. Ulysses' second fast latitude scan: Complexity near solar maximum and the reformation of polar coronal holes. Geophys. Res. Lett. 29, 1290.
Modzelewska, R., Bazilevskaya, G., Boezio, M., Koldashov, S., Krainev, M.B., Marcelli, N., 2020. Study of the 27-day variations in GCR fluxes during 2007–2008 based on PAMELA and ARINA observations. Astrophys. J. 904, 3.
Moeketsi, D.M., Potgieter, M.S., Ferreira, S.E.S., Heber, B., Fichtner, H., Henize, V.K., 2005. Modelling changes in solar wind speed based on time-evolution of polar coronal holes: Implications for the modulation of 3–10 MeV electrons. Adv. Space Res. 35, 597.
Mohlolo, S.T., Engelbrecht, N.E., Ferreira, S.E.S., 2022. A detailed comparison of techniques used to model drift in numerical cosmic ray modulation models. Adv. Space Res. 69, 254.
Moloto, K.D., Engelbrecht, N.E., Burger, R.A., 2018. A Simplified Ab Initio Cosmic-ray Modulation Model with Simulated Time Dependence and Predictive Capability. ApJ 859, 107.
Moraal, H., Potgieter, M.S., 1982. Solutions of the spherically-symmetric cosmic-ray transport equation in interplanetary space. Astrophys. Space Sci. 84, 519.
Moskalenko, I.V., Strong, A.W., Ormes, J.F., Potgieter, M.S., 2002. Secondary antiprotons and propagation of cosmic rays in the galaxy and heliosphere. ApJ 565, 280.
Ngobeni, M.D., Potgieter, M.S., 2010. The heliospheric modulation of cosmic rays: Effects of a latitude dependent solar wind termination shock. Adv. Space Res. 46, 391.
Ngobeni, M.D., Potgieter, M.S., 2011. Modulation of galactic cosmic rays in a north-south asymmetrical heliosphere. Adv. Space Res. 48, 300.
Ngobeni, M.D., Potgieter, M.S., 2015. Modelling the effects of scattering parameters on particle-drift in the solar modulation of galactic cosmic rays. Adv. Space Res. 56, 1525.
Ngobeni, M.D., Aslam, O.P.M., Bisschoff, D., Potgieter, M.S., Ndiitwani, D.C., Boezio, M., Marcelli, N., Munini, R., Mikhailov, V.V., Koldobskiy, S.A., 2020. The 3D numerical modeling of the solar modulation of galactic protons and helium nuclei related to observations by PAMELA between 2006 and 2009. Astrophys. Space Sci. 365, 182.
Ngobeni, M.D., Potgieter, M.S., Aslam, O.P.M., Bisschoff, D., Ramokgaba, I.I., Ndiitwani, D.C., 2021. Numerical modeling of the solar modulation of Helium isotopes in the inner heliosphere. PoS (ICRC2021), 1338.
Ngobeni, M.D., Potgieter, M.S., Aslam, O.P.M., Ramokgaba, I.I., Ndiitwani, D.C., 2022. Simulations of the solar modulation of Helium isotopes constrained by observations. Adv. Space Res. 69, 2330.
Nndanganeni, R.R., Potgieter, M.S., 2016. The energy range of drift effects in the solar modulation of cosmic ray electrons. Adv. Space Res. 58, 453.
Parker, E.N., 1965. The passage of energetic charged particles through interplanetary space. Planet. Space Sci. 13, 9.
Potgieter, M.S., 2000. The heliospheric modulation of cosmic ray protons: role of enhanced perpendicular diffusion during periods of minimum solar modulation. J. Geophys. Res. 105, 18295.
Potgieter, M.S., 2013. Solar modulation of cosmic rays. Living Rev. Solar Phys. 10, 3.
Potgieter, M.S., 2014. Charge-sign dependent effect in the solar modulation of cosmic rays. Adv. Space Res. 53, 1415.
Potgieter, M.S., 2017. The global modulation of cosmic rays during a quiet heliosphere: A modeling perspective. Adv. Space Res. 60, 848.
Potgieter, M.S., Moraal, H., 1985. A drift model for the modulation of galactic cosmic rays. Astrophys. J. 294, 425.
Potgieter, M.S., Aslam, O.P.M., Bisschoff, D., Ngobeni, M.D., 2021. A Perspective on the Solar Modulation of Cosmic Anti-Matter. Physics 3, 1190.
Potgieter, M.S., Vos, E.E., 2017. Difference in the heliospheric modulation of cosmic-ray protons and electrons during solar minimum of 2006 to 2009. Astron. Astrophys. 601, A23.

Potgieter, M.S., Vos, E.E., Boezio, M., De Simone, N., Di Felice, V., Formato, V., 2014. Modulation of galactic protons in the heliosphere during the unusual solar minimum from 2006 to 2009: A modelling approach. Solar Phys. 289, 391.
Potgieter, M.S., Vos, E.E., Munini, R., Boezio, M., Di Felice, V., 2015. Modulation of galactic electrons in the heliosphere during the unusual solar minimum of 2006–2009: A modeling approach. Astrophys. J. 810, 141.
Quenby, J.J., 1984. The theory of cosmic ray modulation. Space Sci. Rev. 1984 (37), 201.
Raath, J.L., Strauss, R.D., Potgieter, M.S., 2015. New insights from modelling the neutral heliospheric current sheet. Astrophys. Space Sci. 360, 2015.
Raath, J.L., Potgieter, M.S., Strauss, R.D., Kopp, A., 2016. The effects of magnetic field modifications on the solar modulation of cosmic rays with SDE-based model. Adv. Space Res. 57, 1965.
Rankin, J.S., Bindi, V., Bykov, A.M., Cummings, A.C., Della Torre, S., Florinski, V., Heber, B., Potgieter, M.S., Stone, E.C., Zhang, M., 2022. Galactic Cosmic Rays throughout the Heliosphere and in the Very Local Interstellar Medium. Space Sci Rev. 218, 42.
Richardson, J.D., Wang, C., 2011. Plasma in the heliosheath: 3.5 years of observations. Astrophys, J. Lett. 734, L21.
Shen, Z.-N., Qin, G., 2018. Modulation of galactic cosmic rays in the inner heliosphere over solar cycles. Astrophys. J. 854, 137.
Shen, Z.-N., Qin, G., Zuo, P.-B., Wei, F., 2019. Modulation of galactic cosmic rays from helium to nickel in the inner heliosphere. Astrophys. J. 887, 132.
Shen, Z.-N., Qin, G., Zuo, P.-B., Wei, F., Xu, X., 2021. Numerical Modeling of Latitudinal Gradients for Galactic Cosmic-Ray Protons during Solar Minima: Comparing with Ulysses Observations. Astrophys. J. Supp. Series 256, 18.
Smith, C.W., Bieber, J.W., 1991. Solar cycle variation of the interplanetary magnetic field spiral. Astrophysical J. 370, 435.
Song, X., Luo, X., Potgieter, M.S., Liu, X., Geng, Z., 2021. A numerical study of the solar modulation of galactic protons and helium from 2006 to 2017. Astrophys. J. 257, 40.
Stone, E.C., Cummings, A.C., McDonald, F.B., Heikkila, B.C., Lal, N., Webber, W.R., 2013. Voyager 1 observes low-energy galactic cosmic rays in a region depleted of heliospheric ions. Science 341, 150.
Stone, E.C., Cummings, A.C., Heikkila, B.C., Lal, N., 2019. Cosmic ray measurement from Voyager 2 as it crossed into interstellar space. Nature Astron. 3, 1013.
Stozhkov, Y., Makhmutov, V., Svirzhevsky, N., 2022. About Cosmic Ray Modulation in the Heliosphere. Universe 8, 558.
Strauss, R.D., Potgieter, M.S., 2014a. Where does the heliospheric modulation of galactic cosmic rays start?. Adv. Space Res. 53, 1015.
Strauss, R.D., Potgieter, M.S., 2014b. Is the Highest Cosmic-Ray Flux Yet to Come?. Solar Phys. 289 (8), 3197.
Sun, X., Hoeksema, J.T., Liu, Y., Zhao, J., 2015. On Polar Magnetic Field Reversal and Surface Flux Transport During Solar Cycle 24. Astrophys. J. 798, 114.
Tomassetti, N., Barão, F., Bertucci, B., Fiandrini, E., Orcinha, M., 2019. Numerical modeling of cosmic-ray transport in the heliosphere and interpretation of the proton-to-helium ratio in Solar Cycle 24. Adv. Space Res. 64, 2477.
Usoskin, I.G., 2017. A history of solar activity over millennia. Living Rev. Solar Phys. 14, 3.
Vos, E.E., Potgieter, M.S., 2015. New modeling results of Galactic proton modulation during the minimum of solar cycle 23/24. Astrophys J. 815, 119.
Vos, E.E., Potgieter, M.S., 2016. Global gradients for cosmic ray protons during the solar minimum of cycle 23/24. Solar Phys. 291, 2181.
Wang, B.-B., Bi, X.-J., Fang, K., Lin, S.-J., Yin, P.-E., 2019. Time-dependent solar modulation of cosmic rays from solar minimum to solar maximum. Phys. Rev. d. 100, 063006.
Zhao, L.-L., Qin, G., Zhang, M., Heber, B., 2014. Modulation of galactic cosmic rays during the unusual solar minimum between cycles 23 and 24. J. Geophys. Res. 119, 1493.
Zhao, L.-L., Adhikari, L., Zank, G.P., Hu, Q., Feng, X.S., 2017. Cosmic Ray Diffusion Tensor throughout the Heliosphere Derived from Nearly Incompressible Magnetohydrodynamic Turbulence Model. Astrophys. J. 849, 88.